Journal of Solid State Chemistry **150,** 233–249 (2000)
doi:10.1006/jssc.1999.8551, available online at http://www.idealibrary.com on IDEAL®

Structure and Magnetism of $Pr_{1-x}Sr_xFeO_{3-\delta}$

H. W. Brinks,* H. Fjellvåg,* A. Kjekshus,*,[1] and B. C. Hauback†

*Department of Chemistry, University of Oslo, P.O. Box 1033 Blindern, N-0315 Oslo, Norway; and †Institute for Energy Technology, N-2007 Kjeller, Norway

Received July 30, 1999; in revised form October 20, 1999; accepted October 22, 1999

Crystal structure, redox, and magnetic properties for the $Pr_{1-x}Sr_xFeO_{3-\delta}$ solid-solution phase have been studied. Oxidized samples (prepared in air at 900°C) crystallize in the $GdFeO_3$-type structure for $0 \le x \le 0.80$, and probably in the $Sr_8Fe_8O_{23}$-type (unpublished) structure for $x = 0.90$. Reduced samples (containing virtually only Fe^{3+}) crystallize as the perovskite aristotype for $x = 0.50$ and 0.67 with randomly distributed vacancies. The Fe^{4+} content increases linearly in the oxidized samples up to $x \approx 0.70$, whereupon it stabilizes at around 55%. Antiferromagnetic ordering of the G type is observed for oxidized samples ($0 \le x \le 0.90$) which show decreasing Néel temperature and ordered magnetic moment with increasing x, while the Néel temperature is nearly constant at $\sim$700 K for reduced samples. Electronic transitions for iron from an average-valence state via charge-separated to disproportionated states are proposed from anomalies in magnetic susceptibility curves in the temperature ranges 500–600 K and 150–185 K. © 2000 Academic Press

Key Words: **praseodymium strontium iron oxide; structure, magnetism, redox; perovskite phases; charge disproportionation.**

I. INTRODUCTION

The perovskite-type ferrites $AFeO_3$ have attracted attention owing to the interesting variation in their magnetic properties which in many cases appear to be related to changes in the average oxidation state and local coordination of iron. Such structure–property information has to a large extent been derived from a combination of diffraction, magnetic susceptibility, and ^{57}Fe Mössbauer spectroscopy studies (1–4).

The average, formal oxidation state of iron can be monitored by replacing the rare earth element (RE) on the ideally 12-coordinated A site with heterovalent substituents, like the alkaline-earth elements (AE), $RE_{1-x}AE_xFeO_3$. However, large amounts of the thereby introduced higher-valence Fe^{4+} can hardly be obtained at normal synthesis conditions, and for samples, e.g., annealed in air, an increasing oxygen nonstoichiometry (δ) develops with increasing AE content, $RE_{1-x}AE_xFeO_{3-\delta}$. The fully oxidized solid-solution system covers samples with formally mixed-valent Fe^{3+} and Fe^{4+} in octahedral coordination. For the partially reduced samples ($\delta > 0$), oxygen vacancies reduce the coordination to square pyramidal or tetrahedral for some of the iron atoms. These variations influence in turn the electronic and magnetic properties. For example, for $La_{1-x}Sr_xFeO_{3-\delta}$ the Néel temperature (T_N) decreases from $\sim$720 to $\sim$70 K when the content of Fe^{4+} increases from 0 to 68% (5).

At low temperatures, certain $RE_{1-x}AE_xMnO_3$ phases exhibit (6) the interesting feature of spacial charge ordering (CO). A recent study on $Pr_{1-x}Sr_xCoO_{3-\delta}$ has revealed a transformation from an orthorhombically deformed perovskite structure for $x \le 0.30$ to a monoclinic structure for $x > 0.30$, probably correlated with changes in the electronic conductivity at $x \approx 0.3$ (7). The occurrence of the monoclinic structure may be taken as an indication of CO on Co; however, this could not be unambigously verified.

Recent Mössbauer studies claim a charge disproportionation for iron(IV) in several perovskite-like phases at low temperatures. Furthermore, the occurrence of the monoclinic structure for $CaFeO_3$ (8) is interpreted as evidence for cooperative ordering of the charges in this material. The findings by transmission electron microscopy on $La_{1-x}Sr_xFeO_3$ also suggest CO on Fe (9). A powder neutron diffraction study of $La_{0.333}Sr_{0.667}FeO_{2.98}$ (4) confirms charge ordering for the unpaired spin density on iron, but not a concomitant ordering in the crystal structure. However, optical investigations of $La_{0.333}Sr_{0.667}FeO_3$ appear to confirm CO on iron below 198 K (10).

All $REFeO_3$ (RE = La–Lu) take the orthorhombic $GdFeO_3$-type structure (11). There is, however, limited information available for the mixed-valent solid-solution phases $RE_{1-x}Sr_xFeO_{3-\delta}$, with the exception of RE = La (5). Hence, there is little experimental evidence on how the reduced size of RE affects the valence states for iron and the possible ordering of oxygen vacancies.

The present study aims at providing an extensive description of the variation in crystal structure and magnetic properties for the $Pr_{1-x}Sr_xFeO_{3-\delta}$ solid-solution phase,

[1] To whom correspondence should be addressed. Fax: +47 22 85 55 65.

0022-4596/00 $35.00

including also the effect of different types of heat treatment. There are large changes in the magnetic ordering temperature as function of Sr content; T_N is 711 K for $PrFeO_3$ (12), whereas $T_N = 134$ K (13) for $SrFeO_3$ ($\delta = 0.00$) and $T_N = 700$ K (1) for $Sr_2Fe_2O_5$ ($\delta = 0.50$) are reported. Particular attention is presently payed to (i) the electronic state of iron in fully oxidized samples, (ii) the possibility of oxygen-vacancy ordering in strongly reduced samples, and (iii) the possible existence of different, closely related perovskite-like phases as a function of Sr content and oxygen nonstoichiometry. The latter point is considered in relation to the $SrFeO_{3-\delta}$ end composition ($x = 1.00$), which exhibits four related structures, cubic simple perovskite for $\delta = 0.00$, tetragonal for $\delta \approx 0.125$, orthorhombic for $0.25 \leq \delta \leq 0.32$ (14), and orthorhombic brownmillerite type for $\delta = 0.50$ (14).

II. EXPERIMENTAL

Synthesis

Pr_6O_{11} was dissolved in hot diluted nitric acid (99.9%, Strem Chem.). Thereafter $SrCO_3$ (98%, Fluka), $Fe(NO_3)_2 \cdot 9H_2O$ (99%, Fluka), and $C_3H_4(OH)(COOH)_3 \cdot H_2O$ (99.5%, Riedel de Haën) in excess (5–10 times the amount of the cations) were added, and the solution was heated at 180°C overnight. The resulting xerogel was X-ray amorphous. The xerogel was fired at 350°C to remove the major part of the carbonaceous species. This precursor was then pressed into tablets and crystallization was carried out at 900°C in air in an alumina container. Prior to the synthesis, Pr_6O_{11} and $SrCO_3$ were treated at 430°C in air to remove any water. The metal content of the iron nitrate hydrate was determined gravimetrically by complete decomposition to Fe_2O_3. All samples referred to in this report were phase pure according to X-ray diffraction.

The samples synthesized according to the described recipe are termed Type I. A second set of samples, Type II, were obtained by treating Type I samples at 1200°C for at least 48 h in 99.99% N_2 atmosphere. Further details on the treatment of the Type II samples are given in the text when pertinent.

X-Ray Diffraction

Powder X-ray diffraction (PXD) data were collected on a Siemens D5000 diffractometer equipped with primary monochromator and position-sensitive detector (PSD), and using Cu$K\alpha_1$ radiation and Si as internal standard. Unit-cell dimensions were determined by least-squares refinements using the UNITCELL program ([15]). Pattern simulation of PXD data were carried out by means of the FULLPROF98 program (16).

High-resolution synchrotron PXD data were collected for $Pr_{0.50}Sr_{0.50}FeO_{3-\delta}$ at the Swiss–Norwegian beam line at ESRF, Grenoble, in capillary geometry using monochromatic photons with wavelength $\lambda = 79.944$ pm.

X-Ray Absorption Near-Edge Spectroscopy (XNES)

XANES was carried out at the Swiss–Norwegian beam line at ESRF, Grenoble.

Neutron Diffraction

Powder neutron diffraction (PND) data were collected with the high-resolution two-axis diffractometer PUS at the JEEP II reactor, Kjeller, Norway. Monochromatized neutrons of wavelengths around 155 pm (slightly different in different experimental cycles) were obtained by reflection from Ge (511) and were detected by two PSD banks, each covering 20° in 2θ. Diffraction data were measured between $2\theta = 10°$ and 130° and were analyzed in steps of $\Delta 2\theta = 0.05°$. The amount of sample was 1–1.5 g. A cylindrical sample holder was used. Typical measurement time was 24 h. Wavelength calibration was done by measurement of an Al_2O_3 standard sample. Low temperatures were obtained by means of a Displex cooling system.

Rietveld refinements were performed using the FULLPROF98 (16) program. Scattering lengths and form factors for Fe^{3+} were taken from the library of the program. A pseudo-Voigt profile function was used, for both PXD and PND data. Different isotropic temperature factors were used for elements of different types. The number of Bragg reflections and variables entering the least-squares refinement are summarized in Table 1.

Magnetic Measurements

Magnetic susceptibility and magnetization studies were performed with an MPMS (magnetic property measurement system; Quantum Design) in the temperature range $5 \leq T \leq 300$ K. Calibration was done by measurements of

TABLE 1
Relevant parameters for Rietveld refinements of PND Data (2400 points)

Space group	*Pnma*	*R*$\bar{3}$*c*	*Pm*$\bar{3}$*m*	*P*4/*nnc*
Bragg reflections	207	68	20	366
Variables	27	16	16	29
Zero point	1	1	1	1
Scale factor	1	1	1	1
Background	6	4	6	6
Profile	6	4	4	6
Temperature factors	3	3	3	3
Unit-cell dimensions	3	2	1	2
Coordinates	7	1	0	10

a Pd-standard sample (from NIST). The zero-field cooled (ZFC) samples were measured on heating in a magnetic field of 1 kOe. Gelatine capsules were used as sample holders. Magnetic susceptibility was furthermore measured with a Faraday balance in the temperature range $300 \leq T \leq 1000$ K. Calibration was done by measurement of an $HgCo(SCN)_4$ standard sample. The samples were sealed under vacuum in spherical silica-glass containers.

Thermal Analyses

Thermogravimetric (TG) analyses were carried out with a Perkin–Elmer 7 series instrument. Silica-glass containers were used as sample holders. Differential scanning calorimetry (DSC) studies were carried out with a Mettler DSC 3000 system.

Oxygen Analyses

The oxidation state of iron was determined by cerimetric titration after dissolution of the samples in hydrochloric acid in closed, argon-flushed glass containers. Mohrs salt was used for reduction of Fe^{4+} to Fe^{3+} and for adjustment of the Ce^{4+} solution.

III. RESULTS

i. Solid Solubility; Effect of Synthesis Conditions on Sample Properties

Samples of $Pr_{1-x}Sr_xFeO_{3-\delta}$ were synthesized with a perovskite-like structure for the entire composition range $0 \leq x \leq 1.00$. The sample quality, as judged from the half widths (FWHM) of Bragg reflections in the PXD patterns, as well as the oxygen stoichiometry, depends strongly on the synthesis conditions (temperature and oxygen partial pressure).

The end composition $PrFeO_3$ takes the $GdFeO_3$-type structure (space group *Pnma*) with $a = 557.8(2)$ pm, $b = 779.0(2)$ pm and $c = 548.8(2)$ pm. The metric is pseudocubic; $a/\sqrt{2} = 394.4$ pm, $b/2 = 389.5$ pm and $c/\sqrt{2} = 388.1$ pm. For Type I samples, the orthorhombic splitting of the reflections in the PXD diagram diminishes considerably with increasing Sr content. For $x < 0.20$, the splitting is easily evident, and unit-cell dimensions for a $GdFeO_3$-type description could be extracted from the PXD data; cf. Fig. 1. However, on the basis of PXD data for $0.20 \leq x \leq 0.30$ only approximate unit-cell dimensions could be extracted, and for $x > 0.30$ cubic unit-cell dimensions were determined as an approximation of the true structure.

The PXD reflections for Type I samples are broad (Fig. 2). Their half widths are typically $FWHM_{(121)} = 0.26°$ [at $2\theta = 33°$; instrumental resolution from Si standard $FWHM_{Si(111)} = 0.06°$]. One may argue that the broadening arises from the pseudocubicity of the material; however, sharper line profiles and indications for splitting would be expected for well-crystalline samples. Hence, internal stress or composition inhomogeneity are more probable causes. Oxygen gradients are not likely to exist in all samples since this type of defect oxides are well known to show considerable oxygen-ion conductivity at the temperatures chosen for the annealing.

Type II samples exhibit extraordinary, sharp Bragg reflections, comparable with the instrumental resolution (Fig. 2, typically $FWHM_{(121)} = 0.07°$). It appears likely that the annealing at 1200°C has stimulated cation diffusion, thus providing materials with fully random distribution of Sr and Pr over the *A* sublattice. Type I samples are hence probably burdened by local variations in Sr/Pr contents, giving rise to internal strain (which is not necessarily isotropic in nature). For lower Sr levels, e.g., $x = 0.20$, the reflections become sharper, but not completely sharp, upon heat treatment. This indicates that tougher annealing conditions are required for Pr-rich samples.

Type II samples with $x = 0.20$ show superstructure reflections in accordance with the $GdFeO_3$-type structure. However, for $x = 0.50$ and 0.67 the unit cell is cubic for as-synthesized samples. On the other hand, these Type II samples can not be directly compared with the corresponding Type I samples since they represent different oxygen stoichiometries. Type II samples are obtained in a partly reduced state, however, they can easily be reoxidized during post treatments.

There are at least three possible structural transitions which could be considered in more detail: (i) the crossover from $GdFeO_3$-type to cubic symmetry (space group $Pm\bar{3}m$) as a function of δ, (ii) the crossover to a tetragonal structure in the vicinity of $x = 0.85$, and (iii) the possibility of a $GdFeO_3$-type to $LaAlO_3$-type ($R\bar{3}c$) transition as a function of x and δ. These variations would be similar to those reported for $La_{1-x}Sr_xFeO_{3-\delta}$, which takes the $GdFeO_3$-type structure for low values of x, and trigonal, tetragonal, and cubic symmetry for higher substitution levels, depending on the oxygen content (5, 20).

Figure 1 shows an almost linear reduction in the unit-cell volume for $0.00 \leq x \leq 0.70$ (Type I samples). Even though Sr is larger than Pr, the introduction of Sr results in a reduced unit-cell volume. The volume can be considered controlled by the network of corner-sharing octahedra, and hence by the interatomic *B*–O distances as well as by the tilt angles (α, β, γ) and the deformations of the octahedra. For a model with ideal octahedra in the $a^+b^-b^-$ tilt system [Glazer's (21) notation] with space group *Pnma* the volume is given as

$$V = 32 d_{B-O}^3 \cos^2\alpha \cos^5\beta \sqrt{1 + \sin^2\beta}.$$

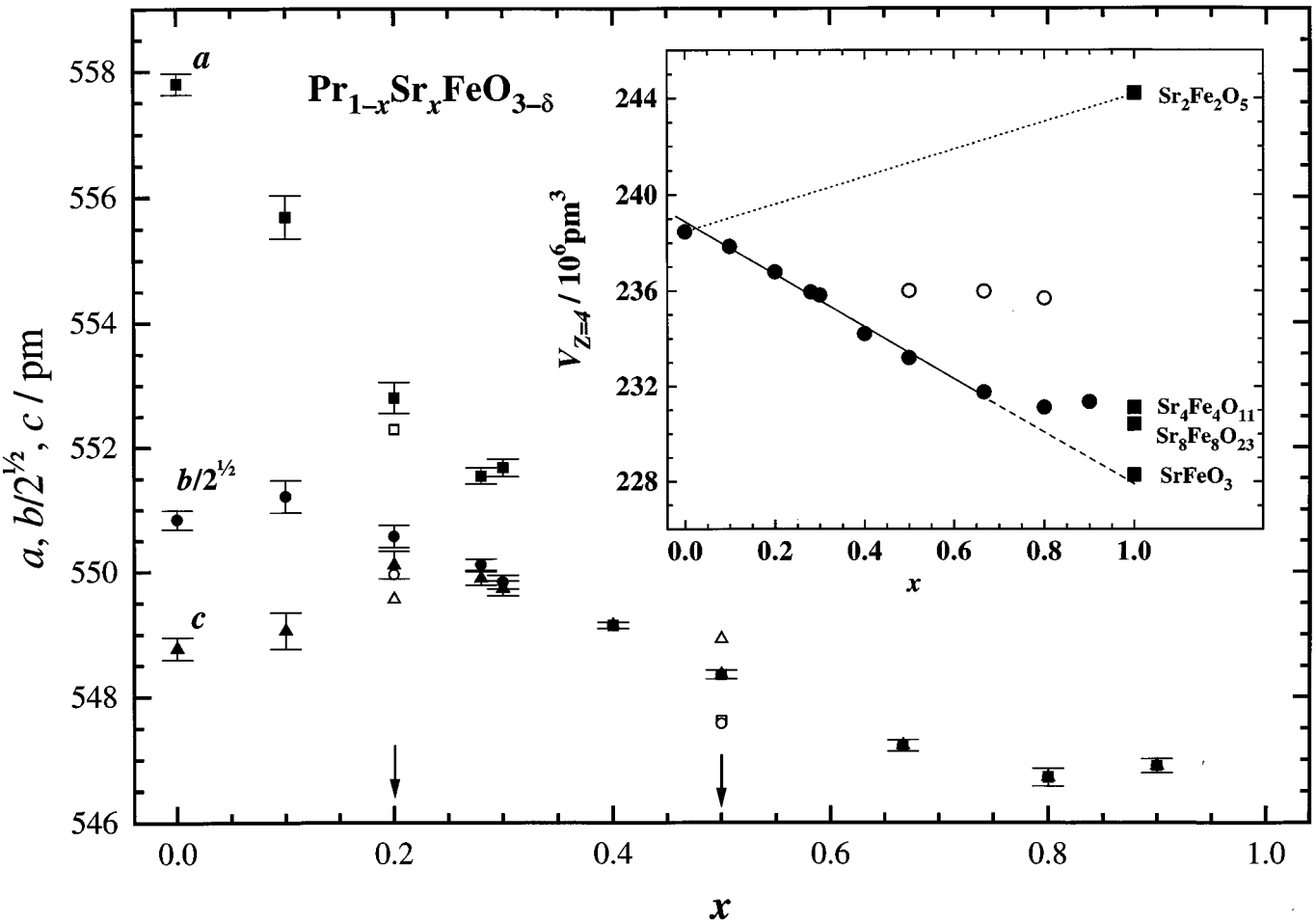

FIG. 1. Unit-cell dimensions (*Pnma* model) for $Pr_{1-x}Sr_xFeO_{3-\delta}$ as a function of the composition parameter x for Type I samples: PXD, filled symbols; PND, open symbols. (Inset) Unit-cell volumes for Type I samples (filled symbols) and Type II samples (open symbols) compared with literature data for $SrFeO_{3.00}$ (17), $Sr_8Fe_8O_{23}$ (18), $Sr_4Fe_4O_{11}$ (18), and $Sr_2Fe_2O_5$ (19).

The size of the A cation does not explicitly enter the expression. However, for A ions like Pr^{3+} that are smaller than oxygen in the ccp stacking of AO_3 layers, introduction of a large cation like Sr^{2+} will induce smaller tilts and thereby a larger volume. On the other hand, in the case of heterovalent substitution, the valence of Fe will increase, and consequently its size will decrease. Therefore, such solid-solution systems will in general reflect the competition between volume decreasing and increasing effects. In $Pr_{1-x}Sr_xFeO_3$ the reduction in the Fe–O distance between $x = 0$ and $x = 0.50$ is large (2.7%) and dominates the overall picture. In the closely related system $Pr_{1-x}Sr_xCoO_3$, the decrease in the Co–O distances is small (0.8% for $x \leq 0.50$) (7) and does not compensate for the decrease in tilt angles caused by the introduction of the larger Sr^{2+} ion.

The leveling off of the $V(x)$ curve in Fig. 1 for $x > 0.70$ is a result of considerable deviations in the oxygen stoichiometry compared with the fully saturated case.

ii. Crystal Structure for $Pr_{1-x}Sr_xFeO_{3-\delta}$, $0.00 \leq x \leq 0.50$

The assignment of the type of deformation of the basic perovskite-type structure was approached by examination of the splitting of the main reflections (PXD, high resolution) and the existence of superstructure reflections (PND, strong O-scattering contribution). The splitting of $\{222\}$ according to a $2 \times 2 \times 2$ superstructure of the basic, cubic perovskite unit cell indicates that $\beta \neq 90°$. This shows that the actual tilt system contains at least two minus tilts (21). The splitting of $\{400\}$ in two reflections with relative intensities 2:1 indicates two similar and one different unit-cell parameter in the superstructure cell, and hence two similar and one different tilt. Superstructure reflections of the type $N = h^2 + k^2 + l^2 = 4C + 3$ (C being an integer) imply that minus tilt is present, while the presence of superstructure reflections with $N = 4C + 1$ shows that both plus and

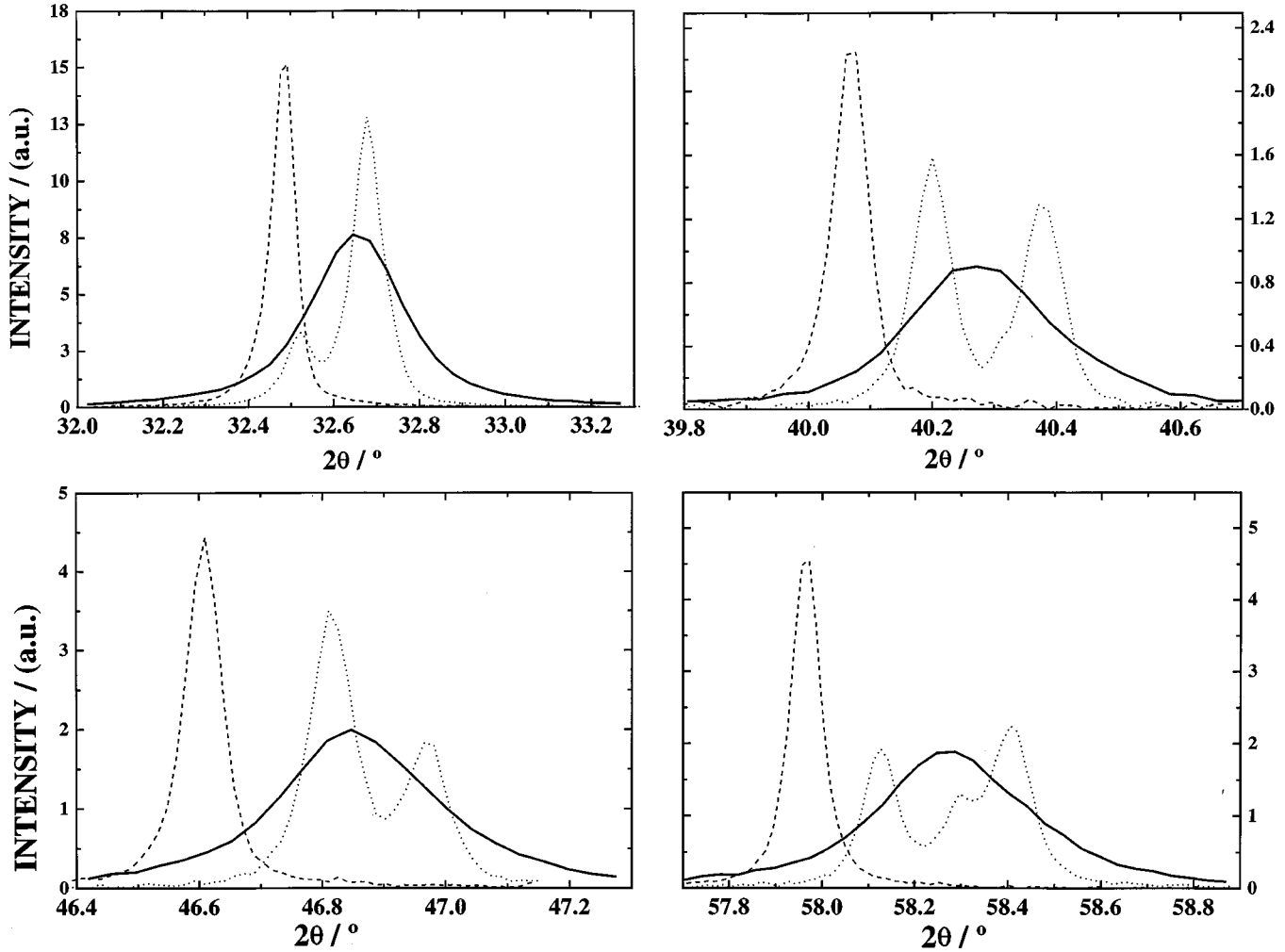

FIG. 2. Representative sections of PXD patterns for $Pr_{0.50}Sr_{0.50}FeO_{3-\delta}$; Type I, thick line; Type II, dashed line; reoxidized Type II, dotted line.

minus tilts are present. According to the Glazer (21) tilt description, there are two possible models $a^+b^-b^-$ and $a^+a^-b^-$, with space groups *Pnma* and $P2_1/m$, respectively —both having unit-cell relations $a/\sqrt{2} \approx b/2 \approx c/\sqrt{2} \approx a_p$. No indication of any monoclinic splitting of this unit cell was seen in the PXD data. Space group *Pnma* and hence the $GdFeO_3$-type structure description was confirmed by means of PND data for $x = 0.20$ (7 and 298 K); see Fig. 3 and Table 2.

The $GdFeO_3$-type description is fully appropriate at low substitution levels of Sr. The splitting of the main reflections and the intensities of the superstructure reflections decrease with increased Sr content. Hence, the deviation from the ideal perovskite-type structure becomes very small with increasing x, which makes it difficult to ascertain the true symmetry. For Type I samples no splitting is observed for $x \geqslant 0.20$; however, superstructure reflections of the types $N = 4C + 1$ and $N = 4C + 3$ are incontestably present in the diffraction patterns right up to $x = 0.80$. PND data for $x = 0.50$ (10 and 298 K) show superstructure reflections of the types $N = 4C + 2$ (plus tilt) and $N = 4C + 3$ (minus tilt), the latter with considerable intensity. The low intensity of $N = 4C + 2$ for the $x = 0.50$ sample compared to the sample with $x = 0.20$ is due to a reduced plus tilt. The third tilt could be zero ($a^0b^+c^-/a^0b^+b^-$, refinements in the common model given by Woodward (22) gave $\chi^2 = 3.20$), plus ($a^+b^+c^-/a^+a^+b^-/a^+b^+b^-/a^+a^+a^-$, $\chi^2 = 3.26$), or minus ($a^+b^-b^-/a^+a^-a^-$, $\chi^2 = 2.92$, $a^+b^-c^-/a^+a^-b^-$, $\chi^2 = 2.82$). The PND data favors the model with two minus tilts and one plus tilt. This conclusion turned out to be fully consistent with PXD synchrotron-radiation data for a sample annealed at 1200°C in air and slowly cooled in the furnace to improve crystallinity. The splitting of {222} indicates two minus tilts, and the splitting of {400} into two reflections implies two equal tilts. This gives two possible tilt systems, $a^+b^-b^-$ and $a^+a^-b^-$. The $a^+b^-b^-$ model with space group

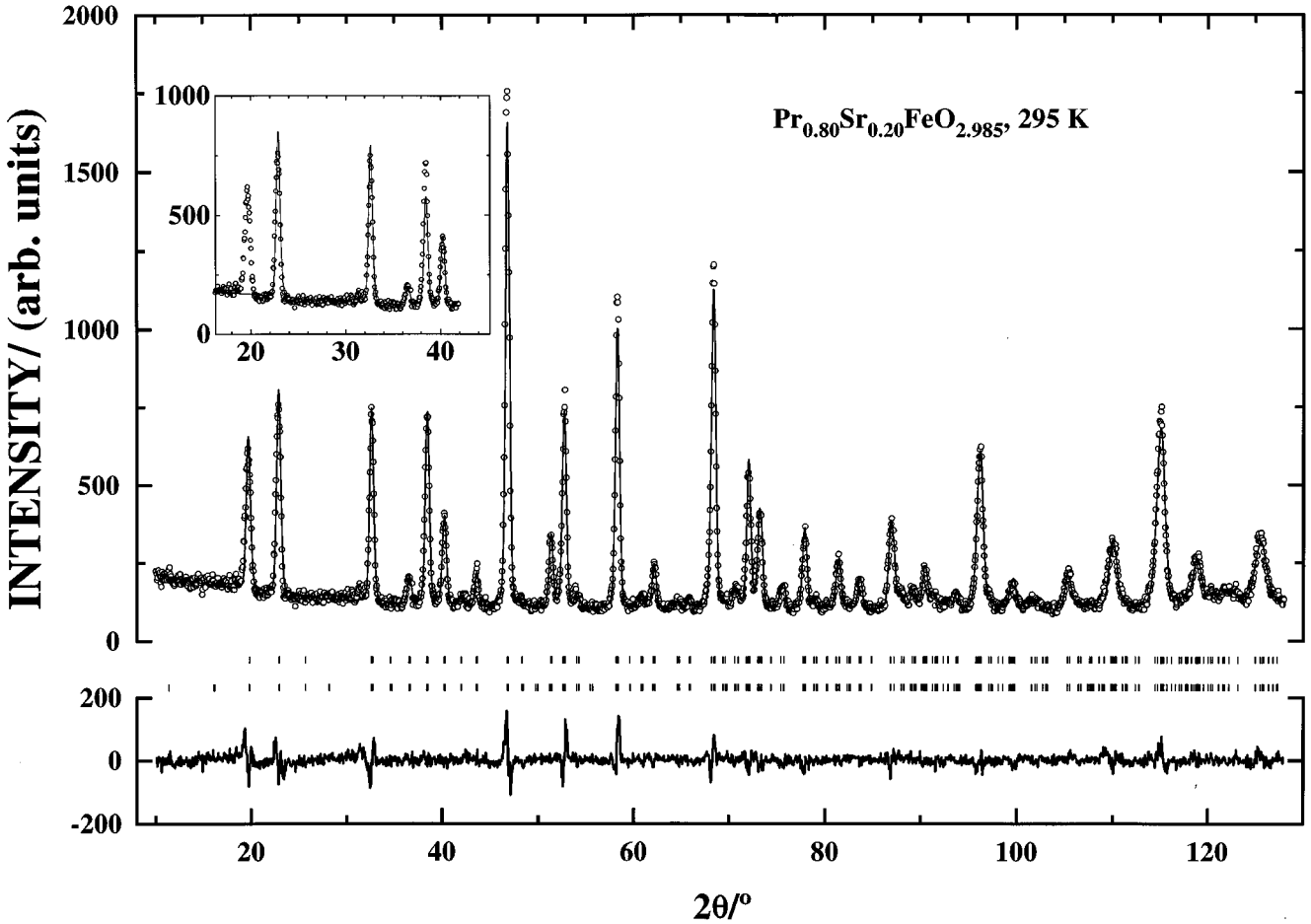

FIG. 3. Rietveld refinements (upper line) of PND data (circles) for $Pr_{0.80}Sr_{0.20}FeO_{2.985}$ (Type I sample). Positions of Bragg reflections are shown with bars for nuclear (upper) and magnetic (bottom) contributions, respectively. The difference between observed and calculated intensity is shown by the bottom line. (Inset) The magnetic contributions illustrated with the deviation of the simulated PND diagram from the observed intensities when only the nuclear structure is taken into account.

Pnma was again chosen, due to its higher symmetry; see Fig. 4 and Table 2.

The samples $x = 0.50$ Type I and reoxidized Type II, as well as that measured by synchrotron-radiation PXD, have the same unit-cell volume, but the splitting of the unit-cell dimensions of the first are smaller than the samples which were synthesized at higher temperature. Rietveld refinements of PND data constrained to the synchrotron-radiation unit-cell dimensions give a significantly worse fit. This phenomenon probably originates from strain on the Pr/Sr site.

Figure 5 shows the variation of a parameter S which measures the deviation from pseudocubic metric. S decreases strongly with x and reaches a constant non-zero level around $x = 0.30$. One may speculate whether the existence of two ranges with quite different deformation parameters S can be taken as a sign of two different structural arrangements. However, S is not an order parameter, since it does not couple directly to the atomic displacements like the shifts of the oxygen atoms which facilitate the octahedral tilts. In conclusion, the present results indicate a $GdFeO_3$-type structure for $0.00 \leqslant x \leqslant 0.50$.

iii. Crystal Structure for $Pr_{1-x}Sr_xFeO_{3-\delta}$, $x = 0.67$

For Type I samples, superstructure reflections of the types $N = 4C + 1$ and $N = 4C + 3$ are present in the diffraction patterns up to $x = 0.80$. This may suggest that the $GdFeO_3$-type structure is retained up to $x = 0.80$. However, in order to evaluate the structural aspects in more detail, it was required that we turned to the Type II samples with much better sample quality.

The composition $x = 0.67$ corresponds to that of the possibly ordered superstructure $PrSr_2Fe_3O_8$. Such a vacancy-ordered superstructure (corresponding to $n = 3$ in the series $A_nB_nO_{3n-1}$ with ordered octahedra and tetrahedra)

TABLE 2
Structural and Magnetic Parameters for $Pr_{1-x}Sr_xFeO_3$ (Type I) According to Rietveld Refinements of PND Data

x, T (K)	0.20, 7	0.20, 295	0.50, 10	0.50, 295
a (pm)	551.92(4)	552.29(5)	546.24(7)	547.62(7)
b (pm)	775.57(6)	777.76(7)	771.74(11)	774.38(13)
c (pm)	548.58(5)	549.56(5)	547.28(7)	548.92(7)
$x_{Pr/Sr}$	0.4731(10)	0.4726(11)	0.4856(13)	0.4856(13)
$z_{Pr/Sr}$	− 0.0036(25)	− 0.0040(26)	− 0.0011(21)	− 0.0041(21)
$x_{O(1)}$	0.0134(11)	0.0145(12)	0.0050(20)	0.0015(18)
$z_{O(1)}$	0.0640(13)	0.0718(16)	0.0735(11)	0.0687(12)
$x_{O(2)}$	0.2870(7)	0.2834(8)	0.2638(17)	0.2638(18)
$y_{O(2)}$	− 0.0433(6)	− 0.0383(7)	− 0.0193(5)	− 0.0163(5)
$z_{O(2)}$	0.2127(8)	0.2157(8)	0.2342(16)	0.2342(17)
$\mu_{AF}(\mu_B)$	3.35(3)	2.98(3)	2.32(3)	1.86(4)
R_p	0.0636	0.0645	0.0594	0.0600
χ^2	1.55	1.28	3.13	2.83

Note. Space group *Pnma* with Pr/Sr in 4*c*, Fe in 4*a*, O(1) in 4*c*, and O(2) in 8*d*. Calculated standard deviations in parentheses.

has been observed for $RESr_2Fe_3O_8$ with RE = La, Dy, Y, Er, Yb, but not for other REs (2). The required synthesis conditions for possibly obtaining such a 3,3,8 phase have to be rather reductive since all the iron has to be trivalent. This condition seems to be fulfilled for Type II samples.

For $x = 0.67$ (Type II) a cubic perovskite-type phase with $a = 389.280(8)$ pm is obtained. FWHM of the reflections corresponded to the instrumental resolution of the diffractometer. PND data showed no additional reflections of structural origin, and excellent fit was achieved by refinement of the crystal structure according to space group $Pm\bar{3}m$. This description implies that there are no tilts of the octahedra. Based on the refined occupation number for oxygen, the composition is $Pr_{0.33}Sr_{0.67}FeO_{2.68}$. The oxygen vacancies are randomly distributed over the O sublattice. Results of the refinements are shown in Table 3.

In order to promote vacancy ordering, the sample was subjected to a second annealing at 800°C in an evacuated, closed silica-glass ampoule (to facilitate approximately the same oxygen content). Some oxygen was released from the sample as seen by the loss of the vacuum condition. However, the sample remained simple cubic, $a = 389.586(8)$ pm, and refinement of PND data gave the oxygen content 2.67(2).

On oxygen saturation in air at 900°C for 24 h and slow cooling, the sample absorbed oxygen, and splitting developed for the still very sharp Bragg reflections. The PND data show additional reflections of the type $N = 4C + 3$. However, it was not possible on the basis of Rietveld refinements alone to unambiguously decide whether the crystal structure remained of the $GdFeO_3$ type, as would be expected from concentration extrapolation from the interval $x \leq 0.50$. The additional reflections could be consistent with both rhombohedral ($R\bar{3}c$, $LaAlO_3$ type) and orthorhombic distortions. Actually, it has recently been reported ([23]) that $PrSr_2Fe_3O_{9-\delta}$ ($\delta < 0.1$) takes the $LaAlO_3$-type structure. By closer consideration of FWHM for the high-resolution PXD data, the variations in the peak widths were analyzed in relation to possible splittings induced by rhombohedral or orthorhombic distortions. The analysis clearly suggests a rhombohedral deformation, e.g., the observed $FWHM_{(220);\,cubic} = 0.206°$, whereas expected widths are 0.194° (rhombohedral case) and 0.128° (orthorhombic case). Results from the refinement of $Pr_{0.33}Sr_{0.67}FeO_{2.94}$ are given in Table 4, and diffraction profiles are given in Fig. 6. Note that the refined rhombohedral distortion is very small, $\alpha = 60.084°$.

iv. Crystal Structure for $Pr_{1-x}Sr_xFeO_{3-\delta}$, $x = 0.90$

The PXD diagram for $x = 0.90$ indicates a cubic pattern with no superstructure reflections exceeding the detection limit (estimated to be 0.35% of the strongest reflection). On the other hand, PND shows a number of additional weak reflections which could be indexed on the tetragonal unit cell with $a = 1090.12(4)$ pm and $c = 767.92(4)$ pm, which is related by $a = 2\sqrt{2}a_p$, $c = 2a_p$ to the basic cubic perovskite unit cell.

The unit cell suggests a close relationship to the recently described superstructure for $Sr_8Fe_8O_{23}$ ($SrFeO_{2.875}$) (18, 24) and also to the so-called 8,8,20 superstructures (25). The present powder diffraction pattern did not allow an unambiguous determination of the space group, but the absent reflections are consistent with, e.g., the highly symmetric space group $P4/nnc$.

The Rietveld refinement converged, but nevertheless, the description should be considered as approximate. The model prescribes random oxygen vacancies around the nonequivalent Fe atoms; furthermore some Fe–O distances become rather short [173 pm, which gives a too large bond valence for Fe(3)], which either indicates shortening owing to unsatisfactory modeling of filled and empty O sites, or wrong symmetry. Superior data are required to solve these open questions. Atomic coordinates are given in Table 5.

Throughout the $Pr_{1-x}Sr_xFeO_{3-\delta}$ solid-solution domain, there exist four related phases with different tilting of the octahedra and/or with oxygen vacancy ordering. Increasing Sr content decreases the structural deviation from the perovskite aristotype and a transition to tetragonal symmetry is observed. Larger δ results in the perovskite aristotype. There are indications of a strain stabilization of the *Pnma* structure model, which is transformed to $R\bar{3}c$ when heat treatment at higher temperatures is applied (for $x = 0.67$).

In $Pr_{0.10}Sr_{0.90}FeO_{2.80}$ there is, assuming that the structure model is correct, a mixture of six-, five-, and fourfold coordination. For comparison, $Sr_2Mn_2O_5$ is reported (26) to have an ordered arrangement of square pyramids and

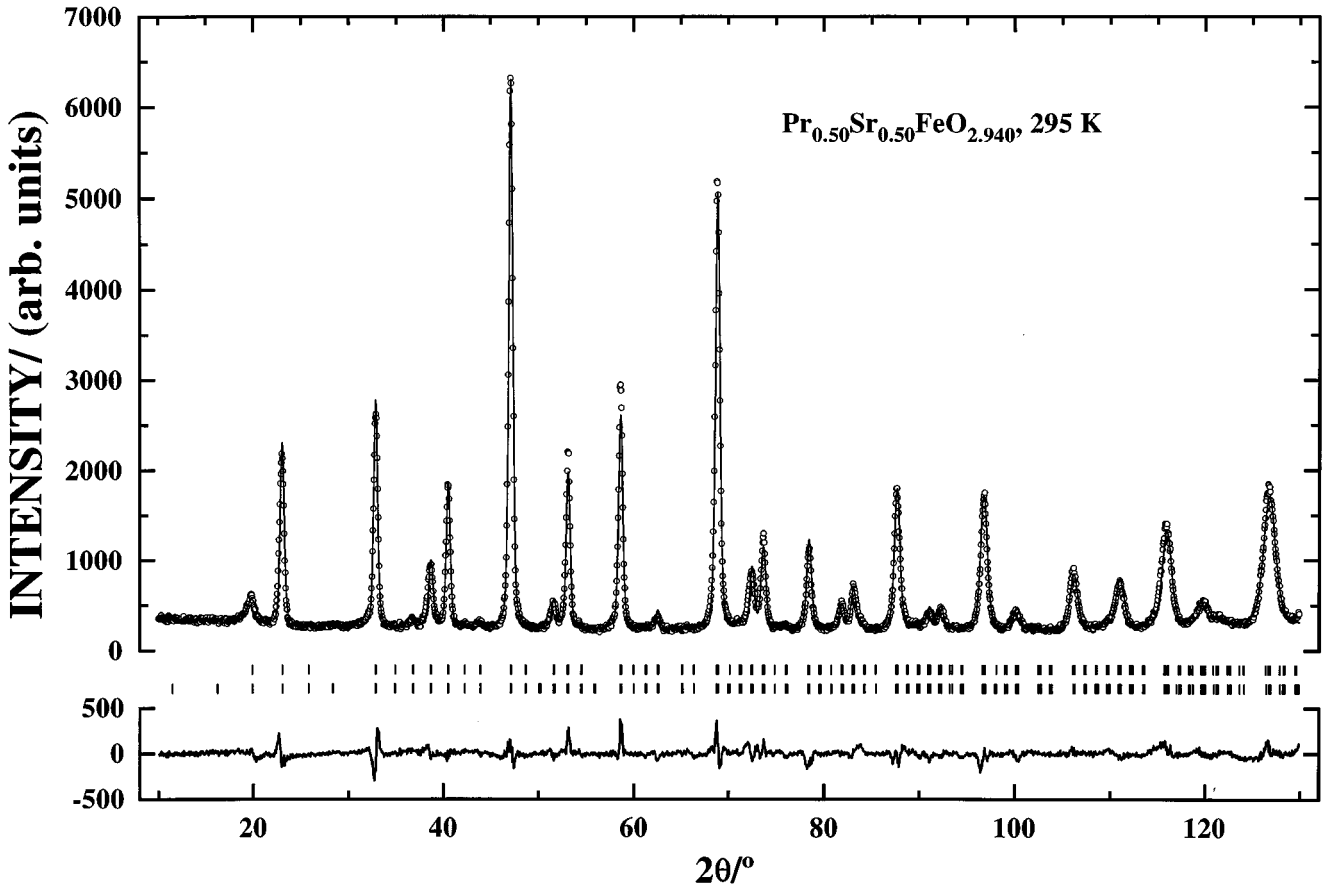

FIG. 4. Rietveld refinements (upper line) of PND data (circles) for $Pr_{0.50}Sr_{0.50}FeO_{2.940}$ (Type I samples). Positions of Bragg reflections are shown with bars for nuclear (upper) and magnetic (lower) contributions, respectively. The difference between observed and calculated intensity is shown by the bottom line.

$SrFeO_{3-\delta}$ to have square pyramids as well, while $LaSr_2Fe_3O_8$ contains ordering of octahedra and tetrahedra (3).

In principle, the samples with $GdFeO_3$ type, $LaAlO_3$ type, and the 8,8,23 superstructure represent distinct phases and should be separated in the phase diagram by solubility gaps, while the $Pm\bar{3}m$ variant can be visualized as reached by a second-order phase transition from the other phases. Owing to the slight differences in the diffraction patterns, any such two-phase region may easily escape detection.

The Type II samples gave a slightly better fit by Rietveld refinement than Type I samples (cf. Figs. 4 and 6). This could be due to strains around the Pr/Sr site, which in turn could give rise to larger uncertainties than expected in the structural parameters. Nevertheless, the presently obtained parameters values for Type I samples are expected to be reliable. Systematic discrepancies between observed and calculated intensities are observed for the groups of reflections with $N = 20$ and 24 for both types of samples. The reason for this is not understood.

v. Bond Distances and Valence Considerations

Selected interatomic distances and bond angles are given for the *Pnma* and $R\bar{3}c$ variants in Table 6. The listed coordination numbers for Pr/Sr refer to bond distances corresponding to bond valences larger than $0.038 \cdot v_{Pr/Sr}$, where v denotes valence (27). On increasing x, the average Pr/Sr coordination is altered, from a square antiprism (CN = 8) for $x = 0.20$ via a cuboctahedron with one empty corner (CN = 11) for $x = 0.50$ to a cuboctahedron (CN = 12) for $x = 0.67$ (Type II, oxidized in air at 900°C and slowly cooled) and 0.90. This is in conformity with the size difference between Pr^{3+} (117.9 pm) and Sr^{2+} (131 pm).

When the average size of the Pr/Sr atoms at the A site increases and approaches the size of O^{2-} (140 pm), the $(Pr,Sr)O_3$ close-packed layers become less deformed, and the size mismatch results in decreasing octahedral tilts. The average Fe–O–Fe angle increases from 157° for $x = 0.20$ via 166° for $x = 0.50$ to 176° for $x = 0.90$, approaching the

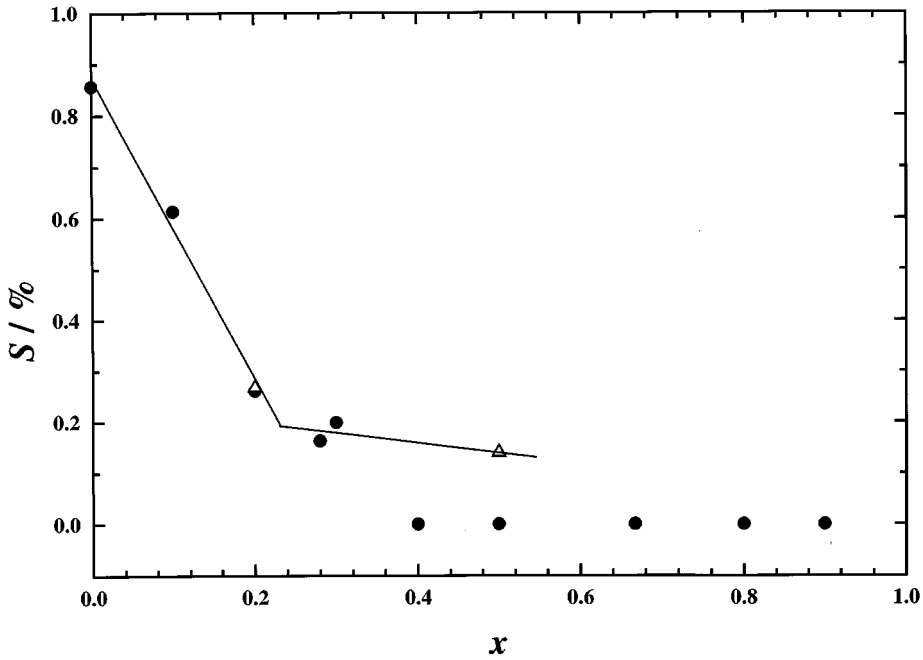

FIG. 5. Relative standard deviation ($S = \sum_{i=1}^{3}(k_i - \bar{k})/2$) of the pseudocubic unit-cell dimensions k_i for PXD (circles) and PND (triangles) data.

value of 180° observed for the cubic phase of the reduced samples of Type II.

Bond valence calculations give a lower value for the Pr/Sr position than prescribed by the formal counting of charges (Table 6). Correspondingly, a too-high valence is calculated for the Fe atoms. On the other hand, the relative change in calculated valence between $x = 0.20$ and 0.67 fits fairly well the expected variation in formal oxidation state for Fe.

vi. Redox Properties

The oxygen nonstoichiometry can be monitored by controlling the temperature and oxygen partial pressure, and can be assessed by redox titrations. This implies that the formal oxidation state of iron can be monitored within the quite broad limits of current interest. For Type I samples prepared in air at $p(O_2) = 0.21$ bar, the Fe^{4+} content increases linearly up to $x \approx 0.70$ whereupon it stabilizes at around 55% (Fig. 7). There is no major difference in behavior between Type I samples of $Pr_{1-x}Sr_xFeO_{3-\delta}$ and $Pr_{1-x}Sr_xCoO_{3-\delta}$ (7).

On turning to high oxygen pressures, $p(O_2) = 180$ bar at 650°C, the Fe^{4+} content can be increased as, e.g., evidenced by decreased unit-cell dimensions. Under such oxidizing conditions only a small nonstoichiometry prevails for $x \leq 0.90$.

TABLE 3

Structural and Magnetic Parameters for $PrSr_2Fe_3O_{8+\delta}$ Type II (a, Annealing at 1200°C in N_2; b, Subsequently Annealed at 800°C in Sealed Silica-Glass Container) According to Rietveld Refinements of PND Data

	Type IIa	Type IIb
T (K)	295	295
a (pm)	389.264(3)	389.671(14)
δ	0.04(5)	0.01(6)
$\mu_{AF}(\mu_B)$	3.13(4)	3.32(4)
R_p	0.0767	0.0770
χ^2	2.46	2.25

Note. Space group $Pm\bar{3}m$ with Pr/Sr in 1*a*, Fe in 1*b*, and O in 3*c*. Calculated standard deviations in parentheses.

TABLE 4

Structural Parameters for $PrSr_2Fe_3O_{8+\delta}$ (Type II, Oxidized in Air at 900°C and Slowly Cooled) According to Rietveld Refinements of PND Data

T (K)	295
a_H (pm)	547.65(4)
c_H (pm)	1338.92(8)
a_R (pm)	546.96
α_R (°)	60.084
x_O	0.5219(3)
δ	0.83(5)
R_p	0.0608
χ^2	1.51

Note. Space group $R\bar{3}c$ (hexagonal setting) with Pr/Sr in 6*a*, Fe in 6*b*, and O in 18*e*. Calculated standard deviations in parentheses.

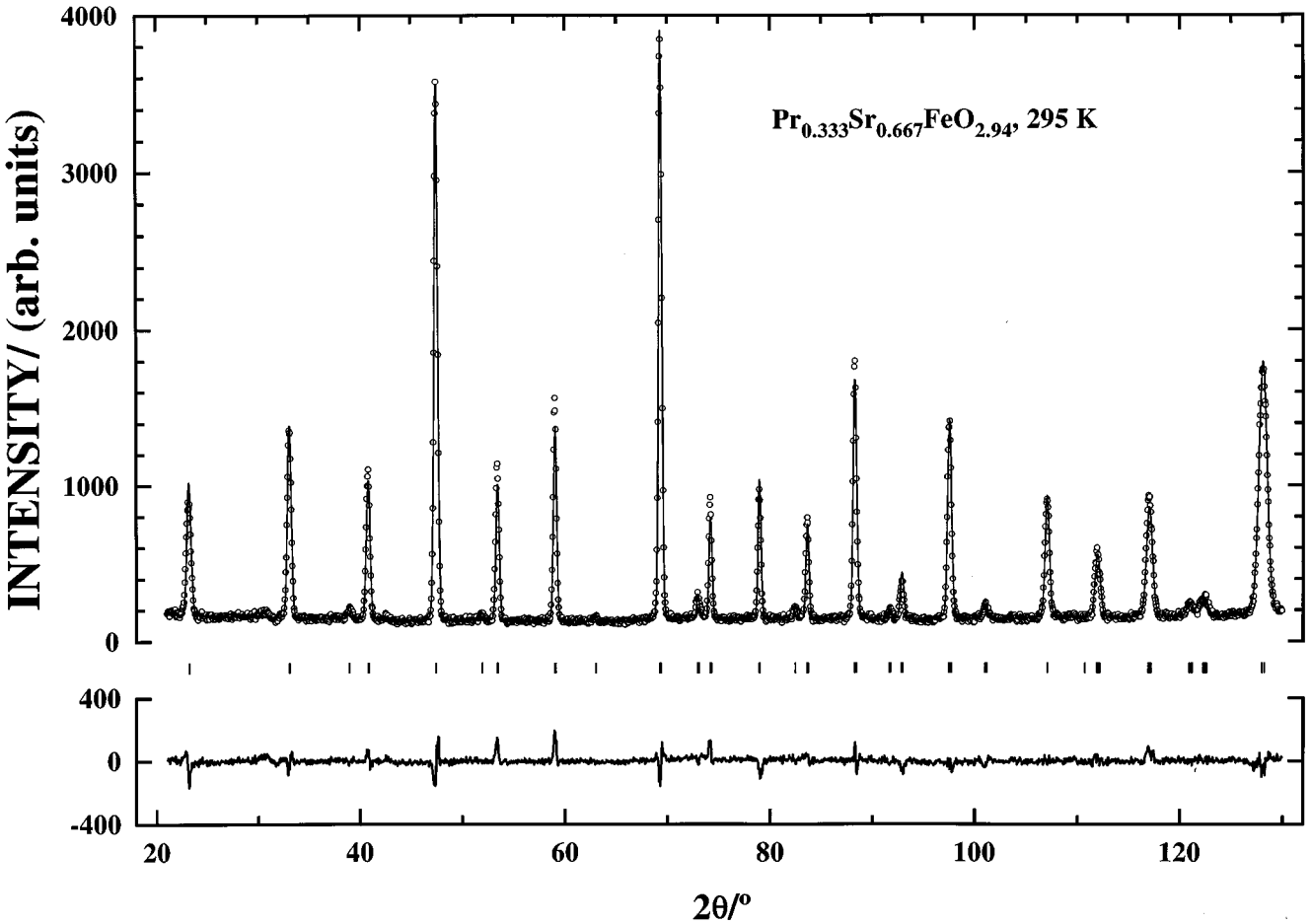

FIG. 6. Rietveld refinements (upper line) of PND data (circles) for $Pr_{0.33}Sr_{0.67}FeO_{2.94}$ (Type II). Positions of Bragg reflections are shown with bars for nuclear (upper) and magnetic (lower) contributions, respectively. The difference between observed and calculated intensity is shown by the bottom line.

In N_2 atmosphere at 1200°C, an oxygen partial pressure of around 10^{-4} bar appears to be about right for obtaining (mainly) trivalent iron in Sr-rich samples. The ideal chemical formula for such Fe^{3+} samples is $Pr_{1-x}Sr_xFeO_{3-x/2}$. For more Pr-rich samples, e.g., $x = 0.50$, the derived unit-cell volume is far lower than that expected from a Vegard law relationship between $PrFeO_3$ and $Sr_2Fe_2O_5$ (see inset to Fig. 1). This may result from attractive interactions between strontium and oxygen vacancies or from improved packing efficiency of FeO_5-square pyramids relative to the packing of FeO_4 tetrahedra. However, it is not likely that the Pr-rich samples can be reduced entirely to the Fe^{3+} state in N_2 atmosphere.

TG experiments show a lower oxygen loss on heating for $Pr_{1-x}Sr_xFeO_{3-\delta}$ than for $Pr_{1-x}Sr_xCoO_{3-\delta}$ (7), and a substantial amount of Fe^{4+} prevails in air at 1000°C. According to TG, the minimum temperature at which oxygen transport into the sample can be observed at a cooling rate of 2 K/min, decreases with x and equals 150°C for $x = 0.67$.

vii. Electronic and Magnetic Properties

The electronic properties of the $Pr_{1-x}Sr_xFeO_{3-\delta}$ solid-solution phase will mirror variations in the formal iron valence (between Fe^{3+} and Fe^{4+}) and the local iron coordination (tetrahedral FeO_4, square pyramidal FeO_5, octahedral FeO_6).

A change in the Fe 3*d* configuration and its local coordination could be expected to influence the XANES spectra. However, for the solid-solution samples with $x \leq 0.90$ and virtually no oxygen nonstoichiometry, there are no major distinctions in the spectra (Fig. 8). For the analogous La phase a corresponding lack of changes has been ascribed (28) to a situation in which the formal Fe oxidation state does not affect 3*d*, but is brought about by the introduction of holes in bands of primarily oxygen character at the Fermi level.

The magnetic properties of $Pr_{1-x}Sr_xFeO_{3-\delta}$ are rather complex. Magnetic order prevails for all x and δ at low

TABLE 5
Structural and Magnetic Parameters for $Pr_{0.10}Sr_{0.90}FeO_{2.80}$ according to Rietveld Refinements of PND Data at 8 K

a (pm)	1090.12(4)
c (pm)	767.92(4)
$x_{Pr/Sr}$	0.9945(5)
$y_{Pr/Sr}$	0.7444(4)
$z_{Pr/Sr}$	0.0153(6)
$x_{Fe(4)}$	−0.0026(4)
$z_{O(2)}$	−0.025(2)
$x_{O(4)}$	0.1254(11)
$x_{O(5)}$	0.877(2)
$x_{O(6)}$	0.8623(9)
$y_{O(6)}$	0.1143(8)
$z_{O(6)}$	0.7643(8)
$\mu_{AF}(\mu_B)$	0.84(9)
R_p	0.068
χ^2	4.3

Note. Space group $P4/nnc$ with Pr/Sr in 16*k*, Fe(1)–Fe(4) in 2*a*, 2*b*, 4*c*, and 8*h*, as well as O(1)–O(6) in 4*d*, 4*e*, 8*f*, 8*h*, 8*h*, and 16*k*, respectively. Calculated standard deviations in parentheses.

temperatures. The ordered moment and the ordering temperature, as well as the paramagnetic properties, depend strongly on the formal Fe oxidation state and short- and long-range crystallographic order of the oxygen vacancies (i.e., local coordination). The available data (5) for the La analog inspire us to regard this as a consequence of the atomic size of the *RE* component. For $Pr_{1-x}Sr_xFeO_{3-\delta}$ we focus on the effect of the increased Fe valence while the octahedral FeO_6 coordination is maintained, and on the effect of changed local coordination while the Fe oxidation state is retained at Fe^{3+}.

For all samples, antiferromagnetic order of G type was observed. The additional reflections of magnetic origin in the PND patterns were in several cases rather weak. However, their existence was easily verified by the Rietveld refinements which revealed additional, nonnuclear scattering contributions at low angles for reflections of the type $N = 4C + 3$. Refined magnetic parameters are given in Table 2, and relevant diffraction data are presented in Fig. 3. The moment direction could not be unequivocally determined owing to the pseudocubic structure and overlapping of reflections; however, a G_z mode appears probable for $x = 0.20$ and 0.50. This is in accordance with the findings for $PrFeO_3$ ([29]).

T_N is certainly a function of both x and δ. For the related $La_{1-x}Sr_xFeO_{3-\delta}$ phase, T_N is reported (5) to be mainly dependent on the Fe^{3+} content. However, the determination of T_N by nondiffraction methods is not simple in such phases. For $PrFeO_3$, $T_N = 690$ K was detected by

TABLE 6
Selected Bond Distances (in pm) and Angles (Degrees) from Rietveld Refinements of PND Data for $Pr_{1-x}Sr_xFeO_{3-\delta}$ Type I and II ($x = 0.667$)

x, T (K)	0.20, 7	0.20, 295	0.50, 10	0.50, 295	0.667, 295, II	0.667, 295, IIb
$d_{Fe-O(1)}$	197	199	197	197	194	195
$d_{Fe-O(2)}$	200	199	195	195	194	195
$d_{Fe-O(2)}$	200	199	193	194	194	195
$d_{Pr/Sr-O}$	238	242	258	260	262	276
	238	242	258	260	262	276
	242	239	234	239	262	276
	256	256	266	268	274	276
	265	266	267	268	274	276
	265	266	267	268	274	276
	276	275	273	273	274	276
	276	275	273	273	274	276
	301	302	287	285	274	276
	308	313	313	310	286	276
	328	324	296	296	286	276
	328	324	296	296	286	276
∠Fe,O(1),Fe	159.0	156.6	156.4	157.9	172.9	180
∠Fe,O(2),Fe	154.3	156.9	168.9	169.9	172.9	180
∠Fe,O(2),Fe	154.3	156.9	168.9	169.9	172.9	180
$CN_{Pr/Sr}$	8	8	11	11	12	12
$d_{Pr/Sr-O}$	257	258	270	271	274	276
d_{Fe-O}	198.8	198.7	195.2	195.5	193.9	194.8
Valence Pr/Sr	2.65[a]	2.57	2.58[a]	2.46	2.37	2.20
Valence Fe	3.24[a]	3.24	3.57[a]	3.54	3.69	3.60

Note. Typical estimated standard deviations for the bond lengths are 2 pm in Fe–O and 6 pm in Pr/Sr–O.
[a] Bond valences are, strictly spoken, only relevant at room temperature.

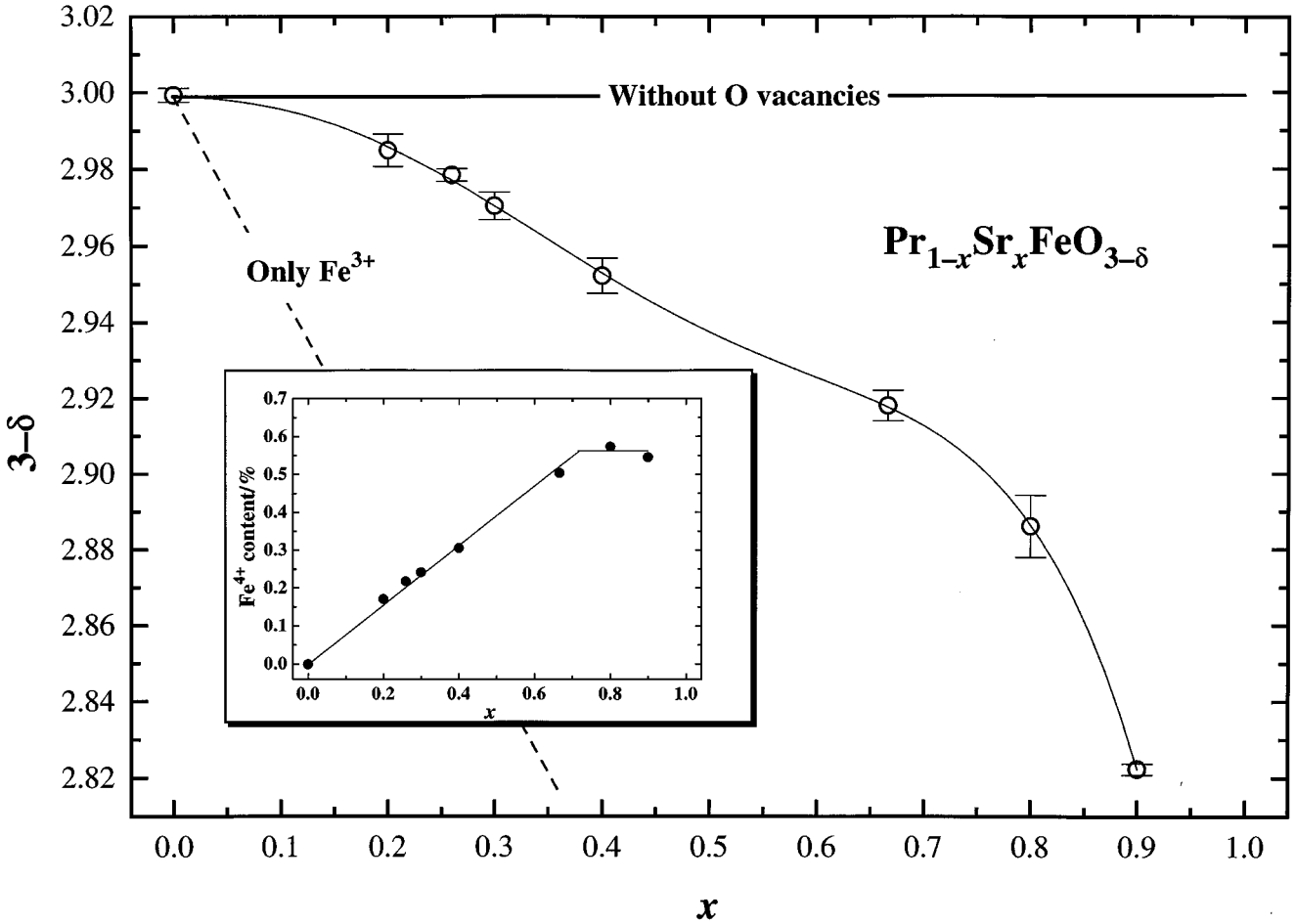

FIG. 7. Oxygen content of $Pr_{1-x}Sr_xFeO_{3-\delta}$ as determined by redox titrations. (Inset) Calculated Fe^{4+} content as a function of x.

means of DSC as a small endothermic peak. A similar observation was made for $LaFeO_3$ (30). The lack of corresponding observations for the substituted samples is probably caused by compositional smearing. For $x = 0.20$ and 0.50, T_N is above 295 K and could be estimated from the decay of the refined magnetic moment (assuming that μ_{AF} follows a Brillouin function) to 590 and 440 K, respectively. For other compositions we had to rely on magnetic susceptibility data (*vide infra*).

Inverse magnetic susceptibility data are shown in Fig. 9 for the temperature range 5 to 1000 K. Field scans at 5 K gave, except for $x = 0$, straight lines confirming that the the samples are in the assumed antiferromagnetic state without a ferromagnetic contribution. For $PrFeO_3$ the small hysteresis is most probably caused by a small intrinsic ferromagnetism. In the paramagnetic regime, these curves represent the sum of independent magnetic contributions from praseodymium and iron. Assuming an $^3H_4$ spectroscopic ground state for Pr^{3+} the paramagnetic moment $\mu_p(Pr^{3+}) = 3.58\ \mu_B$. This causes a substantial paramagnetic background, contributions which prevail down toward 5 K and may blur the detection of T_N for the iron sublattice.

The decrease in T_N with increasing amounts of Fe^{4+} resembles the situation for $La_{1-x}Sr_xFeO_{3-\delta}$, where T_N drops below room temperature when the Fe valence increases above $+3.35$ (5).

For $x = 0.80$, field-dependent susceptibility developed as function of holding time during measurements at around 750 K (Fig. 10). More detailed studies revealed that this phenomenon correlates with T_C for the strongly ferrimagnetic $SrFe_{12}O_{19}$ phase. Judged from the saturation magnetization, the amount of segregated $SrFe_{12}O_{19}$ has to be extremely small, around 30 ppm. The formation of $SrFe_{12}O_{19}$ could indicate that $Pr_{1-x}Sr_xFeO_{3-\delta}$ is metastable in the relevant composition–temperature interval. However, it appears more likely that the minor degrading is induced by a slow reaction between the Sr component of the sample and the silica-glass container. No such problems

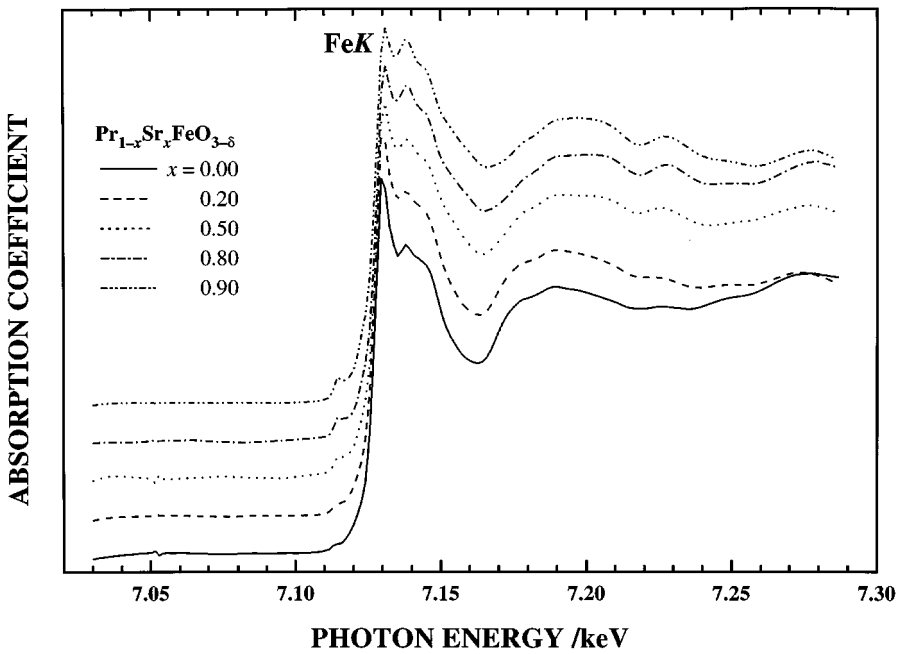

FIG. 8. XANES spectra for selected samples of $Pr_{1-x}Sr_xFeO_{3-\delta}$ for δ corresponding to the appropriate x values in Fig. 7.

were detected for other compositions, and the measured $\chi(T)$ curves for these are therefore believed to represent the intrinsic properties of $Pr_{1-x}Sr_xFeO_{3-\delta}$.

For the almost fully oxidized samples of $Pr_{1-x}Sr_xFeO_{3-\delta}$, (i.e., $\delta \approx 0$) the ordering temperature was estimated as the temperature with onset of substantial deviation from the Curie–Weiss law behavior. For these samples T_N drops from 711 K ($x = 0.00$) (12) via 190 ± 10 K ($x = 0.50$) and 175 ± 10 K for $x = 0.75$ to 140 ± 10 K for 0.90 and 134 K for $SrFeO_3$ (13).

For the reduced samples (Type II) with $\delta \approx x/2$, a considerably higher ordering temperature is observed; e.g., for $x = 0.67$, $T_N \approx 700$ K; see inset to Fig. 10. Compared with $T_N = 711$ K for $x = 0.00$ and 700 K for $x = 1.00$ (1), it is seen that T_N remains virtually unchanged as long as the iron valence stays around three.

Interpretation of the paramagnetic susceptibility data in terms of the Curie–Weiss law is possible in certain temperature intervals for all studied samples. However, most of the samples show anomalies in $\chi(T)$. For the oxidized samples (either in air or under high oxygen partial pressure, *vide infra*) a transition appears to occur around 500–600 K (Fig. 9). For these samples, the effective paramagnetic moment usually decreases from the low- to high-temperature side of this "transition." The derived paramagnetic moments above 600 K are compared with calculated values for different possible iron-spin states in Table 7 (assuming constant Pr^{3+} contributions). The transition can not easily be linked to one particular structural phase transition, since $x = 0.50$ and 0.67 may have different crystallographic states at 295 K (*vide supra*).

A quite different trend is observed for the reduced samples, see, e.g., the data for $Pr_{0.33}Sr_{0.67}FeO_{2.68}$ in the inset to Fig. 10. Two linear $\chi^{-1}(T)$ ranges are observed above and below around 700 K. For $100 < T < 700$ K, $\mu_p = 5.82(3)\ \mu_B$, whereas for $T > 700$ K, $\mu_p = 8.2(3)\ \mu_B$. The data refer to a reduced sample measured in an evacuated sample holder, and no structural transition is likely to occur since the structure is of the simple, cubic perovskite type. Hence, the $\chi^{-1}(T)$ anomaly indicates an electronic transition.

IV. DISCUSSION

i. Magnetic Order

The substantial difference in magnetic properties between oxidized and reduced samples of $Pr_{1-x}Sr_xFeO_{3-\delta}$ is related to changes in the effective charge of iron, to bond overlap between oxygen p orbitals and iron d orbitals, and furthermore to the local iron coordination. There is further a striking variation in the magnetic ordering between the closely related $Pr_{1-x}Sr_xFeO_{3-\delta}$ and $Pr_{1-x}Sr_xCoO_{3-\delta}$ phases, the former exhibits antiferromagnetic order with high T_N, the latter ferromagnetic order with low Curie temperatures.

These variations can be rationalized in terms of dominant superexchange interactions ([31]), communicated via the Fe–O–Fe or Co–O–Co pathway of the corner-sharing polyhedra. This superexchange interaction depends both on the electronic configuration of the cations involved and on the

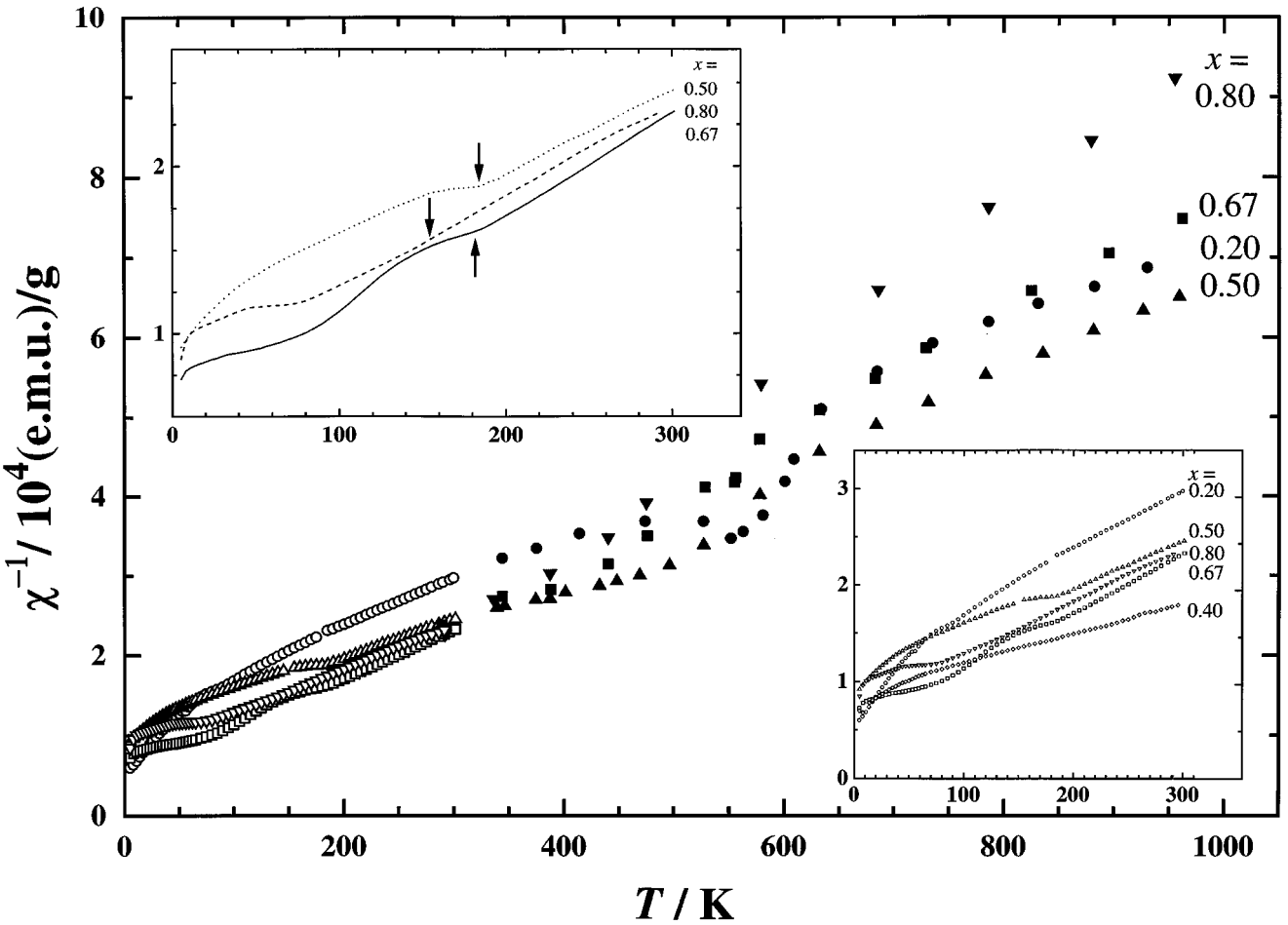

FIG. 9. Inverse magnetic susceptibility for selected samples of $Pr_{1-x}Sr_xFeO_{3-\delta}$ in the temperature range 5 to 1000 K, determined by SQUID (open symbols) and the Faraday (filled symbols) methods. For the oxygen content of the samples see Fig. 7. (Right inset) SQUID measurements of inverse susceptibility below room temperature for $Pr_{1-x}Sr_xFeO_{3-\delta}$. (Left inset) SQUID measurements of inverse susceptiblity below room temperature for some $Pr_{1-x}Sr_xFeO_{3-\delta}$ with probable temperature of charge disproportionation (CD) marked with arrows.

deviation of $\angle$Fe–O–Fe and $\angle$Co–O–Co from 180° (ideal value) as defined through the crystallographic distortions.

Increased Sr-substitution level implies increased amounts of formal Fe^{4+} in the case of the fully oxidized samples of $Pr_{1-x}Sr_xFeO_3$. On the other hand, for reduced samples with $\delta = x/2$, the percentage of Fe^{3+} remains at 100%. The Fe^{3+}–O–Fe^{3+} interaction is strongly antiferromagnetic, and T_N for $Pr_{1-x}Sr_xFeO_{3-x/2}$ remains high and almost unchanged between $PrFeO_3$ and $Sr_2Fe_2O_5$. For the formally mixed-valent oxidized samples, there are strong indications for a charge disproportionation (CD) of Fe^{4+} into Fe^{3+} and Fe^{5+} at low temperatures (*vide infra*). The superexchange mechanism predicts moderate ferromagnetic interactions between Fe^{5+} (t_{2g}^3) and HS Fe^{3+} ($t_{2g}^3e_g^2$) via oxygen (e_g–$p\sigma$–t_{2g}), whereas Fe^{4+}–O–Fe^{3+} and Fe^{5+}–O–Fe^{5+} are weakly antiferromagnetic in character (31). As a whole, T_N is predicted to decrease as the formal Fe^{4+} content increases subject to Sr substitution.

For $Pr_{1-x}Sr_xCoO_{3-\delta}$ it is not possible to provide a straightforward explanation for the ferromagnetism by means of superexchange; LS Co^{3+} is diamagnetic, and furthermore the interactions between two LS Co^{4+} are negligible and those between two HS Co^{4+} are strongly antiferromagnetic. According to Ref. (7), the spin states at low temperatures and low substitution levels are LS Co^{3+} and HS Co^{4+}, which ought to induce antiferromagnetism. Hence, one must either invoke doubleexchange or the more complex superexchange approach suggested by Goodenough for $La_{1-x}Sr_xCoO_{3-\delta}$ (32).

For the related Fe perovskites, magnetic susceptibility measurements for the paramagnetic state and Mössbauer and PND studies have proved Fe^{3+} to be in the HS state (3, 4, 33–35). The same appears to be the case for Fe^{4+}.

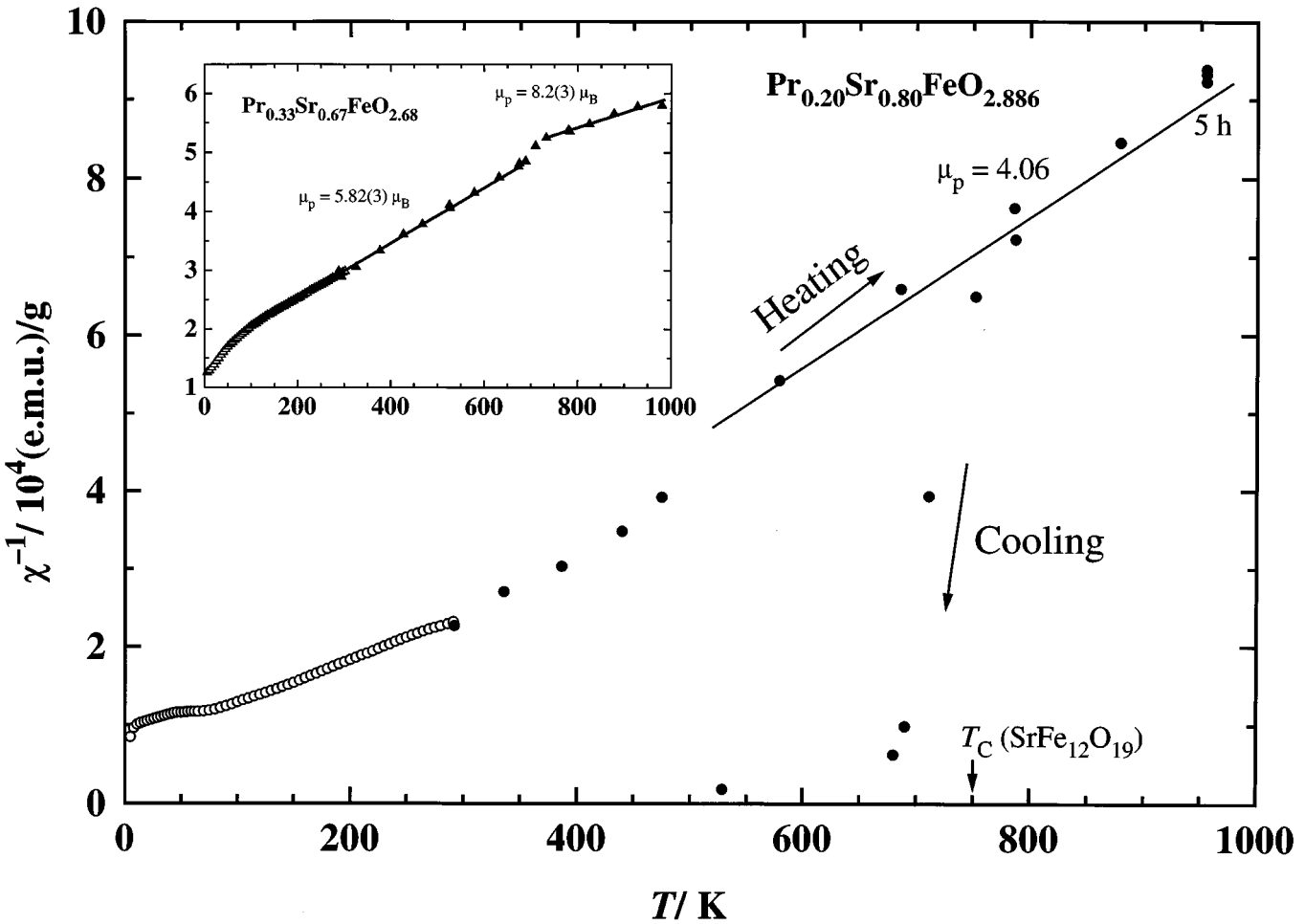

FIG. 10. Inverse magnetic susceptibility of $Pr_{0.20}Sr_{0.80}FeO_{2.886}$ as a function of temperature and heat treatment. T_C for $SrFe_{12}O_{19}$ is indicated. (Inset) Inverse magnetic susceptibility of $Pr_{0.33}Sr_{0.67}FeO_{2.68}$ as a function of temperature, $T_N \approx 700$ K.

The observed antiferromagnetic moment for $Pr_{0.50}Sr_{0.50}FeO_{2.94}$ is far below the value expected for localized HS iron (2.35 vs 4.62 μ_B, assuming spin only) or other possible localized spin-only values. The assumption of localized electrons seems, however, reasonable since the related systems $Dy_{1-x}Sr_xFeO_{3-\delta}$ and $La_{1-x}Sr_xFeO_{3-\delta}$ are reported to be semiconducting, except for the end-composition $SrFeO_{3.00}$ (17, 33, 36, 37).

For the related phase $La_{0.50}Ba_{0.50}FeO_{2.955}$ Mössbauer data indicate HS Fe^{3+} and Fe^{5+}; however, the ordered antiferromagnetic moment of 1.89 μ_B observed by PND is much smaller than the expected spin-only value of 4.59 μ_B (35). Three effects were considered important to account for this observation, reduction of the moments owing to covalency (3.9–4.5 μ_B for Fe^{3+} and 2.0–2.3 μ_B for Fe^{5+}), possible formation of Mattis spin glass, and misalignments of spins (35).

For $Pr_{1-x}Sr_xFeO_3$ the deviation of the ordered moment from a localized spin-only value for HS iron increases from $Pr_{0.80}Sr_{0.20}FeO_{2.985}$ (3.35 vs 4.83 μ_B) to $x = 0.50$ (2.35 vs 4.62 μ_B). The observed reduction in μ_{AF} from $x = 0.00$ [$\mu_{AF} = 4.57$ μ_B for $NdFeO_3$ (38)] to 0.50 fits well the expectations for a Mattis spin-glass system with varying amounts of frustrated spins. In these simple considerations the interaction between Fe^{3+} and Fe^{5+} (which is assumed to be equally distributed on both sublattices) is assumed to be positive, whereas that between irons in the same oxidation states is assumed to be negative in nature.

ii. Low-Temperature Charge Disproportionation (CD)

There are several independent pieces of evidence for charge disproportionation (CD) of Fe^{4+} in perovskite-type oxides at low temperatures. For $CaFeO_3$, CD into Fe^{3+} and Fe^{5+} is reported below 290 K, well above $T_N = 115$ K (34). Convincing Mössbauer spectroscopy data has recently been provided by Nowik *et al.* (23) for $PrSr_2Fe_3O_{9-\delta}$, $\delta < 0.1$. The variations in the hyperfine field and the isomer

TABLE 7
Paramagnetic Moment (μ_p) and Curie Temperature (θ_p) for $Pr_{1-x}Sr_xFeO_{3-\delta}$ in the Indicated Temperature Regions

x	T (K)	$\mu_p(\mu_B)$	θ_p (K)	I $\mu_p(\mu_B)$	II $\mu_p(\mu_B)$	III $\mu_p(\mu_B)$
0.20	685–930	6.20(14)	− 404(41)	6.575	6.376	6.586
0.50	632–659	5.28(4)	− 139(11)	6.085	5.590	6.104
0.67	586–962	4.80(4)	− 70(13)	5.787	5.069	5.808
0.80	579–955	4.02(4)	34(16)	5.570	4.702	5.592

Note. Standard deviations in parentheses. Moments for three spin models (assuming spin-only for iron) are given: I, Fe with a uniform averaged valence in HS state; II HS Fe^{3+} and LS Fe^{4+}; III, HS Fe^{3+} and HS Fe^{4+}.

shift reveal clearly a transition associated with changes in the Fe valences at around 170 K, i.e., slightly below $T_N = 190$ K. Convincing results have furthermore been published by Battle *et al.* (34) for $LaSr_2Fe_3O_{8.94}$, with a first-order electronic transition around 220 K. The hyperfine parameters for the different Mössbauer resonances strongly support the CD equation $Fe^{4+} = Fe^{3+} + Fe^{5+}$.

A different situation dominates at and above room temperature, i.e., above the temperature for the onset of CD. For $PrSr_2Fe_3O_{9-\delta}$ the ^{57}Fe Mössbauer data could best be modeled by assuming the local existence of two distinct Fe valences (23), i.e., Fe^{3+} and Fe^{4+}, and not an average valence. In contrast, Battle *et al.* (34) observed an average-valent Fe for $LaSr_2Fe_3O_{9-\delta}$. This discrepancy could be due to different interpretations of the Mössbauer data or to a real difference between La and Pr. The present XANES data are in accordance with the soft X-ray absorption spectroscopy data (28) for the La phase, which indicated that tetravalent iron remains mainly as d^5 ions, however, accompanied by holes in electron bands of predominantly oxygen character. The differences revealed by Mössbauer and magnetization data around the CD transitions are believed to be related to changes in the 3*d* electron distribution.

No cooperative Jahn–Teller deformation is described for Fe^{4+} in this type of perovskite-type oxides (13, 34, 37). For metallic $SrFeO_{3.00}$ this may be caused by itinerant behavior of the e_g electron (34), whereas for $CaFeO_3$ (34), the Jahn–Teller ion is obviously unstable and CD occurs. On the other hand, the existence of square-pyramidal FeO_5 polyhedra in $SrFeO_{3-\delta}$ (1) could be indicative of static Jahn–Teller deformations for Fe^{4+} (d^4)—by analogy with $Sr_2Mn_2O_5$ (26). However, on the basis of the documented, rather general appearance of CD in these Fe^{4+} systems, one is tempted to ascribe the presence of the type of oxygen-vacancy ordering to a reluctance to stabilize the structure with FeO_4 tetrahedra.

For $PrSr_2Fe_3O_{9-\delta}$ the temperature of CD is determined by Mössbauer spectroscopy to be 170 K (23). In the present study an altered slope in the $\chi^{-1}(T)$ curve is observed at 185 K for $Pr_{0.33}Sr_{0.67}FeO_{2.918}$ (inset to Fig. 9), which may be ascribed to this phenomenon. A similar change is seen in $\chi^{-1}(T)$ for $x = 0.50$ and 0.80 at 185 and 150 K, respectively, but no evidence of a transition is revealed in the DSC curves. For $x < 0.50$ and $x = 0.90$ no signs of CD were observed in the $\chi^{-1}(T)$ curves. A considerable amount of Fe^{4+} is evidently needed to observe the CD transition.

iii. High-Temperature Magnetic Susceptibility

The anomalies in $\chi(T)$ observed around 600 K (Fig. 9), indicate electronic changes, possibly connected with structural changes. On the basis of parallel syntheses of samples using $SrCO_3$ in excess, it can be ruled out that the anomalies are caused by impurities like $SrFe_{12}O_{19}$. They are hence considered intrinsic. Furthermore, they most probably do not reflect CD since this phenomenon is restricted to relatively low temperatures.

At temperatures above the CD range either a transformation in a uniform average-valence state or a charge-separated state with Fe^{3+} and Fe^{4+} takes place (4, 23, 34, 35). The Mössbauer data indicate that iron in $PrSr_2Fe_3O_{9-\delta}$ adopts a state with two distinct iron valences (23). In the average-valence case the paramagnetic moment can be estimated for the probable HS state to be $2[S(S+1)]^{1/2}$, with $S = 1/2(8 - \nu_{Fe})$ where ν denotes valence. This was shown to be a good approximation for $La_{0.33}Sr_{0.67}FeO_{2.98}$ (5.55 vs 5.24 μ_B) (34). For the present samples of $Pr_{1-x}Sr_xFeO_{3-\delta}$ the average-valence model fits reasonably well only at low x (Table 7).

At higher Sr-substitution levels ($Pr_{1-x}Sr_xFeO_{3-\delta}$) it is reasonable to assume existence of a charge-separated state with Fe^{3+} and Fe^{4+} at room temperature (*vide supra*). It is proposed that on further increase in temperature, a transition from this charge-separated state to an average-valence state occurs and that it is this change which is reflected in the $\chi^{-1}(T)$ anomalies at 500–600 K.

ACKNOWLEDGMENT

H.W.B. is grateful to The Research Council of Norway for financial support. The authors are grateful for skillful assistence from the SNBL team, Grenoble, in the collection of powder diffraction and XANES data.

REFERENCES

1. P. D. Battle, T. C. Gibb, and S. Nixon, *J. Solid State Chem.* **79,** 75 (1989).
2. P. D. Battle, T. C. Gibb, and S. Nixon, *J. Solid State Chem.* **79,** 86 (1989).
3. P. D. Battle, T. C. Gibb, and P. Lightfoot, *J. Solid State Chem.* **84,** 237 (1990).
4. P. D. Battle, T. C. Gibb, and P. Lightfoot, *J. Solid State Chem.* **84,** 271 (1990).

5. A. Wattiaux, J. Grenier, M. Pouchard, and P. Hagenmuller, *J. Electrochem. Soc.* **134,** 1718 (1987).
6. A. P. Ramirez, P. Schiffer, S-W. Cheong, C. H. Chen, W. Bao, T. T. M. Palstra, P. L. Gammel, D. J. Bishop, and B. Zegarski, *Phys. Rev. Lett.* **76,** 3188 (1996).
7. H. W. Brinks, H. Fjellvåg, A. Kjekshus, and B. C. Hauback, *J. Solid State Chem.* **142,** 464 (1999).
8. S. Morimoto, T. Yamanaka, and M. Tanaka, *Physica B* **237–238**, 66 (1997).
9. J. Q. Li, Y. Matsui, S. K. Park, and Y. Tokura, *Phys. Rev. Lett.* **79,** 297 (1997).
10. T. Ishikawa, S. K. Park, T. Katsufuji, T. Arima, and Y. Tokura, *Phys. Rev. B* **58,** 13326 (1998).
11. M. Marezio, J. P. Remeika, and P. D. Dernier, *Acta Crystallogr. B* **26,** 2008 (1970).
12. D. Treves, *J. Appl. Phys.* **36,** 1033 (1965).)
13. T. Takeda, Y. Yamaguchi, and H. Watanabe, *J. Phys Soc. Jpn.* **33,** 967 (1972).
14. J. Mizusaki, M. Okayasu, S. Yamauchi, and K. Fueki, *J. Solid State Chem.* **99,** 166 (1992).
15. B. Noläng, Program UNITCELL, Version 0.9, Institute of Chemistry, University of Uppsala, Uppsala, Sweden, 1997.
16. J. Rodriguez-Carvajal, FULLPROF98, Version 0.2, March 1998, ILL, Grenoble, France.
17. J. B. MacChesney, R. C. Sherwood, and J. F. Potter, *J. Chm. Phys.* **43,** 1907 (1965).
18. Y. Takeda, K. Kanno, T. Takada, O. Yamamoto, M. Takano, N. Nakayama, and Y. Bando, *J. Solid State Chem.* **63,** 237 (1986).
19. M. Harder and H. Müller-Buschbaum, *Z. Anorg. Allg. Chem.* **464,** 169 (1980).
20. S. E. Dann, D. B. Currie, M. T. Weller, M. F. Thomas, and A. D. Al-Rawwas, *J. Solid State Chem.* **109,** 134 (1994).
21. A. M. Glazer, *Acta Crystallogr. A* **31,** 756 (1975).
22. P. M. Woodward, *Acta Crystallogr. B* **53,** 32 (1997).
23. I. Nowik, I. Felner, and V.P.S. Awana, *J. Magn. Magn. Mater.* **192,** 67 (1999).
24. H. Fjellvåg, unpublished.
25. L. Er-Rakho, C. Michel, and B. Raveau, *J. Solid State Chem.* **73,** 514 (1988).
26. V. Caignaert, N. Nguyen, M. Hervieu, and B. Raveau, *Mater. Res. Bull.* **20,** 479 (1985).
27. D. Altermatt and I. D. Brown, *Acta Crystallogr. B* **41,** 240 (1985).
28. M. Abbate, F. M. F. de Groot, J. C. Fuggle, A. Fujimori, O. Strebel, F. Lopez, M. Domke, G. Kaindl, G. A. Sawatzky, M. Takano, Y. Takeda, H. Eisaki, and S. Uchida, *Phys. Rev. B* **46,** 4511 (1992).
29. H. Pinto and H. Shaked, *Solid State Commun.* **10,** 663 (1972).
30. S. Stølen, F. Grønvold, H. Brinks, T. Atake, and H. Mori, *J. Chem. Thermodynam.* **30,** 365 (1998).
31. J. B. Goodenough, "Magnetism and the Chemical Bond." Interscience, New York, 1963.
32. J. B. Goodenough, *J. Phys. Chem. Solids* **6,** 287 (1958).
33. M. Takano, J. Kawachi, N. Nakanishi, and Y. Takeda, *J. Solid State Chem.* **39,** 75 (1981).
34. P. D. Battle, T. C. Gibb, and S. Nixon, *J. Solid State Chem.* **77,** 124 (1988).
35. P. D. Battle, T. C. Gibb, P. Lightfoot, and M. Matsuo, *J. Solid State Chem.* **85,** 38 (1990).
36. H. Watanabe, *J. Phys. Soc. Jpn.* **12,** 515 (1957).
37. C. H. Yo and E. S. Lee, *J. Solid State Chem.* **73,** 411 (1988).
38. W. C. Koehler, O. E. Wollan, and M. K. Wilkinson, *Phys. Rev.* **118,** 58 (1960).